






Metastable liquid immiscibility in the 2018–2021 Fani Maoré lavas as a mechanism for volcanic nanolite formation

Simon Thivet ^{1,2✉}, Luiz Pereira ¹, Nicolas Menguy³, Étienne Médard ⁴, Pauline Verdurme⁴, Carole Berthod^{5,6}, David Troadec⁷, Kai-Uwe Hess¹, Donald B. Dingwell ¹ & Jean-Christophe Komorowski ⁶

Nanoscale liquid immiscibility is observed in the 2018–2021 Fani Maoré submarine lavas (Comoros archipelago). Heat transfer calculations, Raman spectroscopy, scanning and transmission electron microscopy reveal that in contrast to thin (500 μm) outer rims of homogeneous glassy lava (rapidly quenched upon eruption, $>1000\text{ }^\circ\text{C s}^{-1}$), widespread liquid immiscibility is observed in thick (1 cm) inner lava rims (moderately quenched, $1\text{--}1000\text{ }^\circ\text{C s}^{-1}$), which exhibit a nanoscale coexistence of Si- and Al-rich vs. Ca-, Fe-, and Ti-rich melt phases. In this zone, rapid nanolite crystallization contrasts with the classical crystallization process inferred for the slower cooled ($<1\text{ }^\circ\text{C s}^{-1}$) lava interiors. The occurrence of such metastable liquid immiscibility at eruptive conditions controls physicochemical characteristics of nanolites and residual melt compositions. This mechanism represents a common yet frequently unobserved feature in volcanic products, with the potential for major impacts on syn-eruptive magma degassing and rheology, and thus on eruptive dynamics.

¹Ludwig-Maximilians-Universität, Department of Earth and Environmental Sciences, 80333 Munich, Germany. ²Department of Earth Sciences, University of Geneva, Geneva, Switzerland. ³Sorbonne Université, Muséum National d'Histoire Naturelle, CNRS, Institut de Minéralogie, de Physique des Matériaux et de Cosmochimie, 75005 Paris, France. ⁴Laboratoire Magmas et Volcans, Université Clermont Auvergne, CNRS, IRD, OPGC, 63178 Aubière, France.

⁵Observatoire Volcanologique et Sismologique de la Guadeloupe, Institut de physique du globe de Paris, 97113 Gourbeyre, France. ⁶Université Paris Cité, Institut de Physique du Globe de Paris, CNRS, 75005 Paris, France. ⁷Institut d'Electronique de Microélectronique et de Nanotechnologies, Université de Lille, 59655 Villeneuve d'Ascq, Lille, France. ✉email: simon.thivet@unige.ch

Liquid immiscibility is a thermodynamic state characterized by the coexistence of two or more immiscible melt phases of distinct compositions¹. It was long thought to occur only at temperatures irrelevant to magmatic and volcanic processes². In subsequent experimental petrology studies however, the potential of natural magma compositions to exhibit liquid immiscibility at super- to sub-liquidus conditions has been well-documented^{3–7}. Currently, liquid immiscibility is suspected to be the cause of major petrogenetic processes, such as the genesis of carbonatitic melts⁸ and hydrothermal systems⁹, as well as the origin of compositional variations of major magmatic intrusions¹⁰ and even the origin of the Daly gap¹¹. Although liquid immiscibility has been described in volcanic products at macro- to micro-scales^{12,13}, it has been rarely documented and characterized at the nanoscale¹⁴.

The very nature of magmatic/volcanic crystallization can be expected to be significantly different in an emulsion (i.e., immiscible system) compared with a homogeneous liquid, largely because of inherited compositional variations¹⁵. Thus, the nanoscale nature of such emulsion can be expected to be an enhancement of the generation of specific nanoscale crystalline phases, termed nanolites¹⁶. However, such a mechanism has not been yet described in detail in natural volcanic products. Instead, an increasing number of studies have reported the characteristic occurrence of nanolites within more typical homogeneous liquids, especially in juvenile tephra deposits^{17–19}. In a purely physical analysis, the direct impact of the presence of isolated nanolites should not play a significant role in magma suspension rheology. However, nanolite clustering, Si-poor phase crystallization, and subsequent Si enrichment in the residual melt can lead to drastic increases in magma viscosity^{20–24}. Further, it has also been shown that these crystals play a role in supporting further heterogeneous nucleation processes such as bubble nucleation, with their consequences for magma fragmentation and, in turn, eruptive dynamics^{24,25}. Indeed, recently, nanolites in submarine volcanic products from the Havre 2012 rhyolitic eruption have been inferred to be the trigger and indicator of unexpected magma fragmentation²⁶.

The present work focuses on textural and associated chemical heterogeneities identified in submarine basanitic volatile-bearing lavas (dissolved H₂O of 1.2 wt.%²⁷), which were erupted during the 2018–2021 Fani Maoré eruption²⁸, ca. 50 km offshore east of Mayotte Island (France), the easternmost island of the Comoros archipelago (Mozambique Channel, Fig. 1a). This eruption represents the largest submarine eruption ever monitored to date with a total estimated lava volume of ca. 6.6 km³ (emplaced between 2.5 and 3.3 km b.s.l., corresponding to an eruptive pressure of 0.29–0.33 kbar)²⁸. This volcanic activity has aroused a lot of interest, giving extensive insights into the origin and characteristics of this major eruption and associated products^{27–31}, as well as the complex aspects of the active volcanic area^{32–35}. Here, we specifically investigate the nanoscale features of the Fani Maoré lava matrixes, which show an evolution from homogeneous to heterogeneous textures, due to nanoscale liquid immiscibility and associated crystallization. More specifically, macroscopic observations, heat transfer calculations, scanning electron microscopy (SEM), Raman spectroscopy, and transmission electron microscopy (TEM) investigations have been used to deduce under which conditions nanoscale liquid immiscibility occurs, and how it affects crystallization as a newly described mechanism for volcanic nanolite generation. Ultimately, we discuss how this mechanism may potentially reveal dynamic processes occurring during volcanic eruptions.

Results

Lava sample descriptions and estimated quenching/cooling rates. Studied lava samples were dredged during the

following oceanographic campaigns: MAYOBS1³⁶, MAYOBS2³⁷, and MAYOBS15³⁸ (Fig. 1b). Five samples have been specifically chosen, which cover the evolution of Fani Maoré eruption in time and space³¹. MAY01-DR0101 sample is from the central edifice and was emitted during the eruptive phase 1, from June 2018 to May 2019, corresponding to the main building stage of Fani Maoré. MAY02-DR0801 and MAY02-DR080102 samples were collected on the peripheral lava flows emplaced in June 2019 during the eruptive phase 2. Finally, MAY15-DR1501 and MAY15-DR150301 samples were dredged on a complex lava flow field that occurred between August 2019 and May 2020 during the eruptive phase 3. Fani Maoré lavas are relatively homogeneous in composition, they are relatively aphyric (<5 vol.% of 20–1000 μm euhedral to skeletal olivines and magnetites formed during magma transport in the crust), with an average porosity of 35 vol.%²⁹. Their basanitic composition (Fig. 1c) represents a complex evolution controlled both by fractional crystallization and mixing between a rising mantle basanitic magma and a static subcrustal tephri-phonolitic magma³¹. The ratio of non-bridging oxygens to tetrahedrally coordinated cations (NBO/T), which represents a proxy for melt polymerization, is calculated for each studied sample, using bulk rock composition³⁹ and assuming a typical Fe oxidation ratio for basanite (Fe³⁺/Fe²⁺) of 0.3⁴⁰. These calculations led to estimated NBO/T values ranging between 0.7 and 0.8 (cf. Supplementary Data 1), which are slightly higher than recent estimations for experimental scenarios at atmospheric conditions which consider all Fe as oxidized in rock compositions⁴¹. NBO/T values of 0.5 were also found using residual melt compositions from previously performed microprobe analyses on slightly crystallized matrices³¹.

All selected samples are part of lava flow margin blocks ca. 5 to 10 cm thick. Three main facies have been identified from macroscopic observations, as well as SEM and Raman transects on the MAY15-DR150301 sample (Fig. 2). Moreover, according to heat transfer calculations using the semi-infinite solid thermal approach⁴², the corresponding average eruptive quenching/cooling rate of lava in contact with seawater as a function of lava thickness/depth can be estimated from the eruptive temperature ($T_E = 1095\text{ °C}$ ²⁹) to the glass transition temperature range ($T_G = 500\text{--}600\text{ °C}$, which represents the viscous to brittle transition of the lava, threshold below which crystallization and degassing cannot occur anymore²⁷). Note that latent heat of crystallization is shown to have an insignificant impact on the lava quenching/cooling rates when compared to the total heat released during cooling (cf. Supplementary Information SI1).

- (1) Outer lava rims, ca. 500 μm thick (cf. area 1 in Fig. 2a), exhibited relatively high eruptive quenching rates greater than ca. 1000 °C s⁻¹ (cf. area 1 in Fig. 2b), yielding a translucent glassy brown macroscopic appearance. This minimum value is coherent with estimated quenching rates by calorimetric relaxational geospeedometry on submarine, fine (i.e., 30–80 μm of diameter) basaltic shards (i.e., 10⁵ °C s⁻¹)⁴³. These outer lava rims are highly fractured, either via thermal stresses in these hyper-quenched volcanic glasses⁴⁴, or due to sampling methodology and sample selection bias (dredging). Thus, the original thin lava rims were difficult to sample. However, rare, thin outer lava rims are identifiable and specifically investigated here from the MAY15-DR1501 sample.
- (2) Inner lava rims are considered as ca. 1 cm thick (cf. area 2 in Fig. 2a). They exhibited moderate quenching rates between ca. 1 and 1000 °C s⁻¹ (cf. area 2 in Fig. 2b), yielding an adamantine yet opaque macroscopic appearance (i.e., slight crystallization). This range is also consistent with estimated quenching rates by geospeedometry on

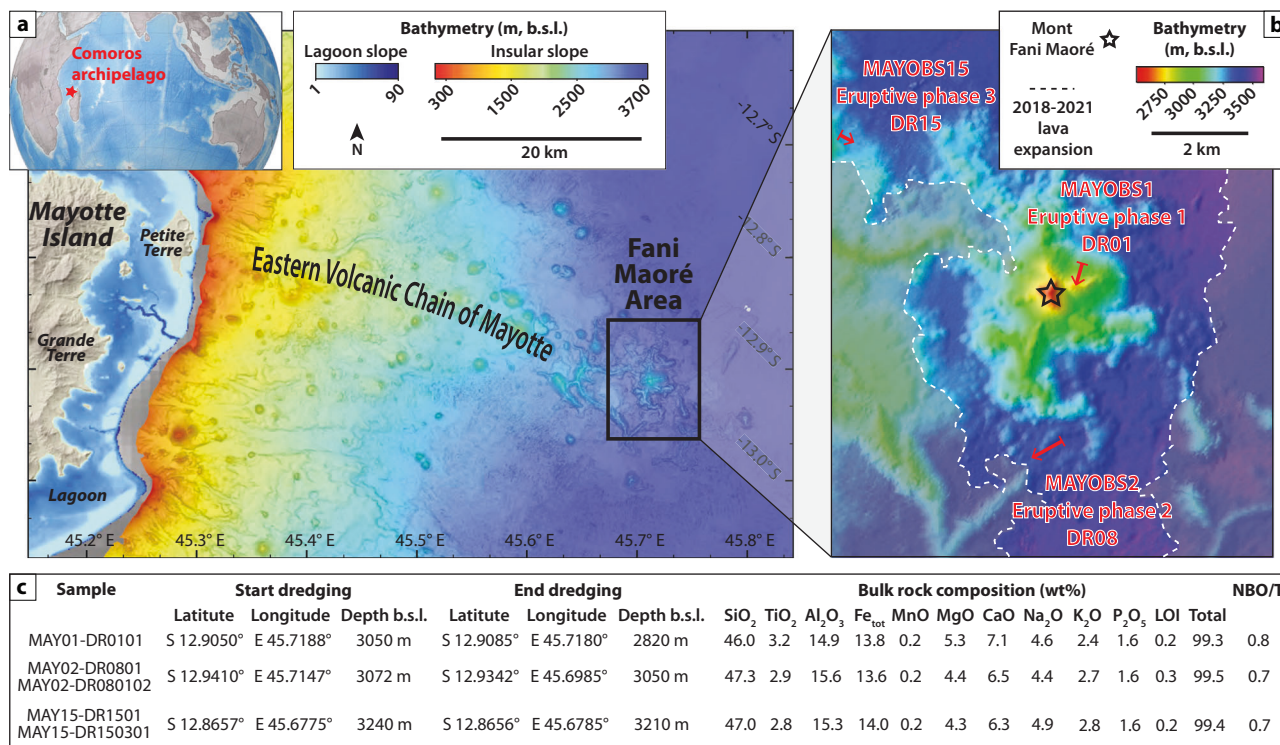


Fig. 1 Map and description of the studied area. **a** Location of the Comoros archipelago and a bathymetric map of the eastern slope of Mayotte Island (France). **b** Zoom on the Fani Maoré volcano area. Red lines show the dredging lines corresponding to the investigated samples, with ending arrows indicating dredge directions. **c** List of the studied samples, with dredging locations and bulk rock compositions²⁹. The ratio of Non-Bridging Oxygens to Tetrahedrally coordinated cations (NBO/T) is also displayed for each sample (cf. Supplementary Data 1).

submarine, coarse (i.e., 0.08–0.12 cm) basaltic shards (i.e., $10^2 \text{ }^\circ\text{C s}^{-1}$)⁴³, confirming the validity of the calculations. Inner lava rims are specifically studied here from the MAY01-DR0101 and MAY02-DR080102 samples.

- (3) Lava interiors correspond to areas located more than ca. 1 cm away from the lava margin (cf. area 3 in Fig. 2a). They underwent slow cooling rates below ca. $1 \text{ }^\circ\text{C s}^{-1}$ (cf. area 3 in Fig. 2b), likely favoring pervasive crystallization and volatile degassing/percolation⁴⁵, yielding a matte and opaque macroscopic appearance with the occurrence of irregularly shaped vesicles. They are specifically studied here from the MAY02-DR0801 sample.

Back-scattered electron images acquired by SEM (BSE-SEM) show that the outer lava rims form a glassy area without any apparent crystallization (cf. image 1 in Fig. 2c), coherently with the previous observations. In contrast, the inner lava rims show slight microlite crystallization and widespread nanoscale matrix heterogeneities (cf. image 2 in Fig. 2c). Within the lava interiors, the matrix tends to be progressively more crystalline with well-defined microlites and nanolites (cf. image 3 in Fig. 2c).

Qualitative Raman spectra analysis acquired from 50 to 1300 cm^{-1} are consistent with this textural evolution. Raman signatures obtained in the outer lava rims (cf. area 1 in Fig. 2d) are characterized by the presence of a peak at ca. 75 cm^{-1} . The changes in this low-wavenumber intensity of Raman spectra can be interpreted as resulting in a shift/intensity change of the Boson peak⁴⁶, which is a typical signature of the glassy state⁴⁷ that tends to disappear in the presence of significant crystalline phases⁴⁸. Also, the absence of any peaks in the $600\text{--}700 \text{ cm}^{-1}$ Raman shift range excludes the abnormal presence of Fe⁴⁹ in this area. In contrast, Raman spectroscopic signatures from the inner lava rims (cf. area 2 in Fig. 2d) show that the low-wavenumber peak at ca. 75 cm^{-1} is no longer well-defined due to the interference with

secondary signals, likely originating from amorphous and/or crystalline nanoscale heterogeneities in this area. In addition, a slight rise of the Raman spectrum between 600 and 700 cm^{-1} suggests the significant presence of Fe that can be either amorphous (i.e., Fe clustering before the actual formation of objects definable as nanolites) and/or crystalline (i.e., occurrence of one or more Fe-bearing nanolite phases)⁵⁰. Within the lava interiors (cf. area 3 in Fig. 2d), Raman signatures show that the low-wavenumber peak at ca. 75 cm^{-1} is absent, most likely due to crystallization and the progressive disappearance of glass. Well-identified peaks between 600 and 700 cm^{-1} also suggest the significant presence of Fe-bearing crystalline phases.

In the following sub-sections, the three lava facies identified above, as well as their corresponding textures are described. It is important to note that these three different facies, observed in the MAY15-DR150301 sample (a full transect description of the sample, illustrated by BSE-SEM images is available in the Supplementary Information SI2), occur consistently in all studied Fani Maoré lava samples (cf. Supplementary File 1) and are thus considered as ubiquitous textures in these eruptive products. For practical reasons involving sample preparation, specific samples were chosen for each case: case 1 (MAY15-DR1501), case 2 (MAY01-DR0101 and MAY02-DR080102), and case 3 (MAY02-DR0801) are representatives of the outer lava rim, inner lava rim, and lava interior textures of the Fani Maoré eruption, respectively.

Case 1: Efficiently quenched outer lava rims. BSE-SEM images and Raman spectra acquired on outer lava rims from the MAY15-DR1501 sample (cf. Supplementary Data 2) reveal signatures similar to those shown in area 1 Fig. 2c, d, confirming the general occurrence of these glassy facies. Unfortunately, TEM analysis

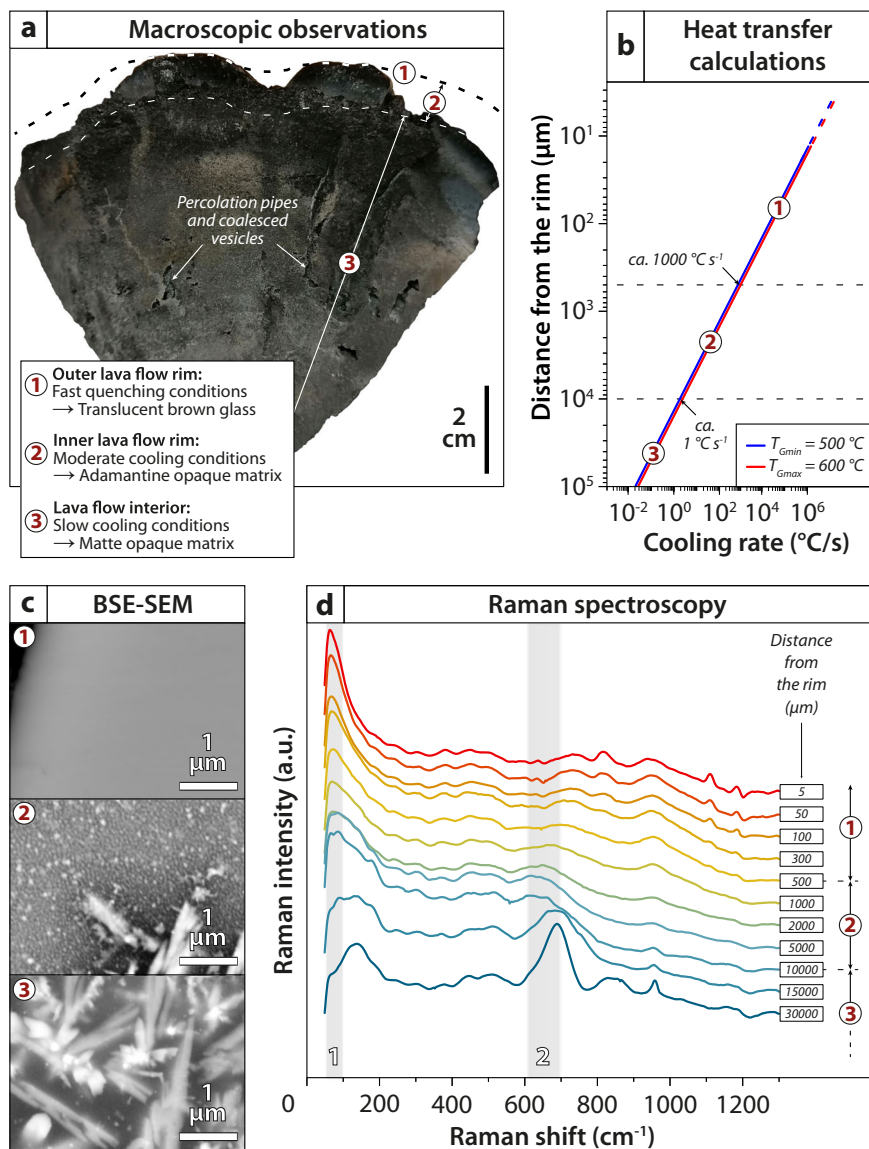


Fig. 2 Lava samples description with estimated quenching rates. **a** Photo of a representative dredge lava sample from the Fani Maoré eruption. Areas 1, 2, and 3 delimit the different lava flow facies and studied areas. **b** Calculated average quenching/cooling rates as a function of lava thickness. T_{Gmin} and T_{Gmax} represent respectively the minimum and the maximum of glass transition temperature of the Fani Maoré samples²⁷. **c** Back-scattered electron images acquired by SEM (BSE-SEM) for each lava facies on the MAY15-DR150301 sample. **d** Uncorrected Raman spectra acquired at different distances from the lava flow margin of the MAY15-DR150301 sample. Gray areas 1 and 2 correspond to the range in which the signature of the Boson peak is typically observed and to the most intense band representative of the occurrence of Fe clustering (amorphous and/or crystalline), respectively.

could not be performed on that area because it was too thin and difficult to work with to make any usable thin section.

However, qualitative Raman spectroscopy and SEM analysis confidently suggest that this area is glassy and homogeneous. This highlights the fact that pre-eruptive melts from the Fani Maoré eruption were homogeneous, microlite- and nanolite-free, and have been efficiently quenched (i.e., $>ca. 1000 \text{ }^\circ\text{C s}^{-1}$) to glass within the first $ca. 500 \text{ }\mu\text{m}$ outer lava rims.

Case 2: Fast nanolite crystallization induced by liquid immiscibility in the inner lava rims. Observations made on the inner lava rims reveal more complex textures, characterized by micro-scale/nanoscale crystalline phases and heterogeneities. Two distinct matrix textures are described below.

BSE-SEM images acquired on the inner lava rims of sample MAY02-DR080102 (Fig. 3a) show that, in addition to the pre-existing pre-eruptive micro-phenocrysts, small ($<ca. 20 \text{ }\mu\text{m}$ in

length) acicular to dendritic microlites and nanolites occur in this sample area. Moreover, the background matrix is characterized by ubiquitous well-structured nanoscale heterogeneities. Raman spectra performed on the matrix (cf. Supplementary Data 2) show signatures similar to those shown in area 2, Fig. 2d, confirming the presence of amorphous and/or crystalline Fe-rich heterogeneities in this facies. High-Angle Annular Dark Field images acquired by Scanning Transmission Electron Microscopy (HAADF-STEM, Fig. 3b), reveal that this lava matrix is dominated by a nanoscale binodal-type liquid immiscibility. The binodal unmixing is characterized by a two-liquid immiscibility field, in which the volumetrically minor immiscible melt phase nucleates and grows as droplets within the volumetrically dominant immiscible melt phase that remains as a continuous matrix phase¹. These sub-round droplets have equivalent spherical diameters from 50 to 200 nm, with rare coalesced droplets having a maximum equivalent diameter of 300 nm. Both

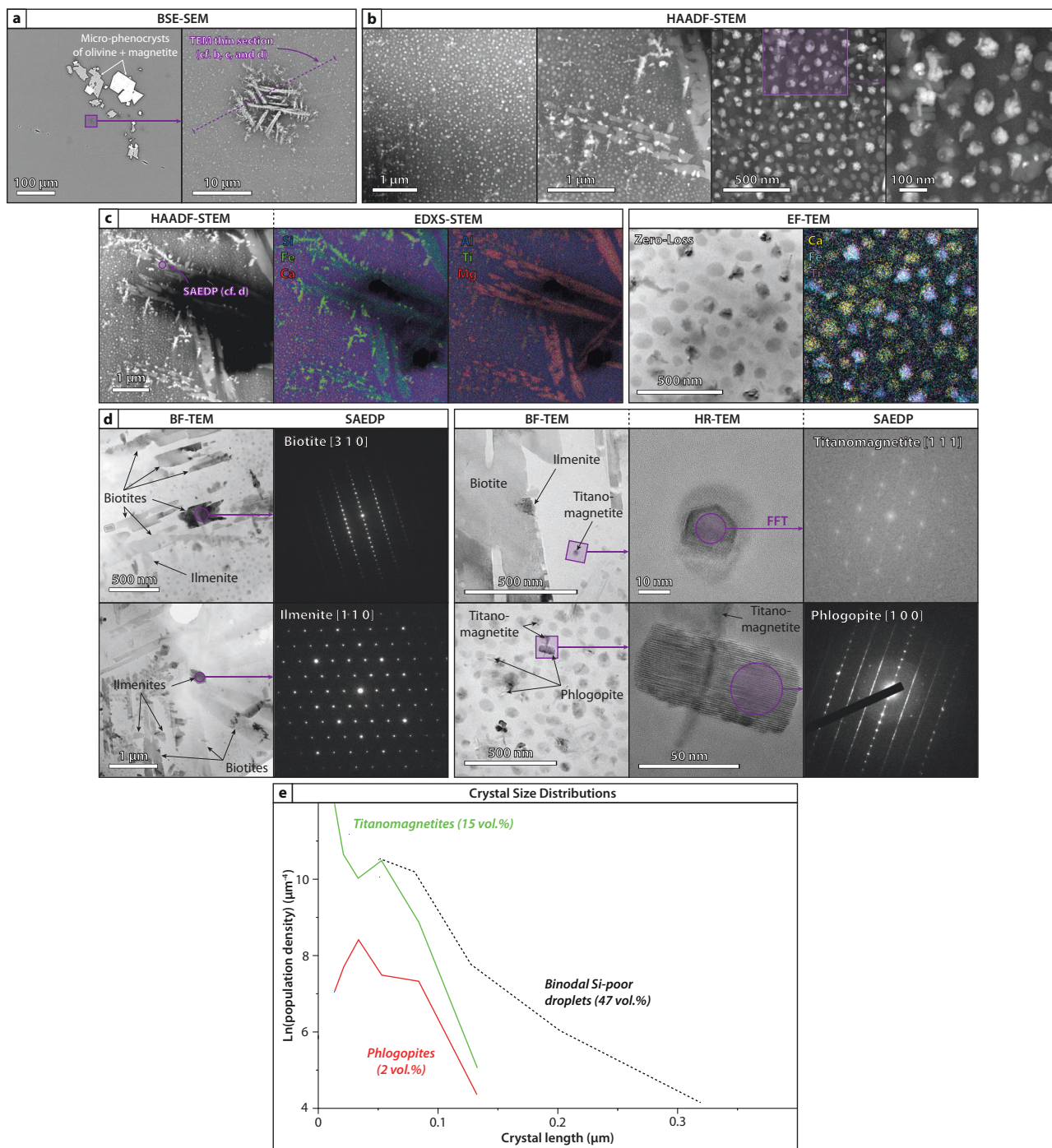


Fig. 3 Textural and chemical investigations made on the inner lava rim of the MAY02-DR080102 sample, representative of binodal-type texture. **a** BSE-SEM images. **b** High-angle annular dark field images acquired by scanning transmission electron microscopy (HAADF-STEM). **c** Reconstructed chemical maps from energy-dispersive X-ray spectroscopy acquired by scanning electron microscopy (EDXS-STEM) and energy-filtered by transmission electron microscopy (EF-TEM). **d** Sample mineralogy characterized by bright-field and high-resolution images acquired by TEM (BF-TEM and HR-TEM), with associated selected area electron diffraction patterns (SAEDP). Note that the SAEDP from the titanomagnetite was reconstructed from the fast fourier transform (FFT) of the associated HR-TEM image. **e** Crystal size distribution (CSD) analysis performed on the acquired HAADF-STEM images.

immiscible melt phases exhibit partial nanoscale crystallization. These nanolites tend to nucleate at the interface between the two melt phases (sometimes resulting in highly deformed droplets) and on other simultaneously formed nanolites, thereby generating rounded aggregates of nanolites (Fig. 3b). Energy-dispersive X-ray spectroscopic analyses acquired by scanning electron microscopy (EDXS-STEM) enable the identification of the micro-crystalline phases (Fig. 3c): acicular microlites are Mg-, Fe- and

Al-rich silicate crystals, which act as nucleation site for smaller (<1 μm) Fe- and Ti-rich crystals. Binodal droplets are enriched in Ca, Fe, and Ti, while the remaining background matrix is enriched in Si and Al. No clear patterns are identified for P, Na, K, Mg, and Mn. In addition to EDXS-STEM data, images from energy-filtered by transmission electron microscopy (EF-TEM) enable an even better resolution of chemical mapping (Fig. 3c). They highlight that uncrystallized parts of the binodal droplets

are Ca-rich, while crystallized parts of the binodal droplets are Fe- and Ti-rich, in agreement with the EDXS-STEM data. Bright-field and high-resolution images acquired by TEM (BF-TEM and HR-TEM), as well as associated selected area electron diffraction patterns (SAEDP) were acquired to determine the mineralogy of this sample area (Fig. 3d): micro-crystalline acicular laths are biotites and smaller crystals that nucleate on them are ilmenites, in agreement with the chemical characterization made by EDXS-STEM. Looking further at the binodal-type texture, euhedral to anhedral titanomagnetite nanolites are observed in the binodal droplets while euhedral to anhedral phlogopites are observed in the background matrix, in agreement with the chemical characterization made by EF-TEM. Crystal size distributions (CSD) highlight that the phlogopite population is less developed (2 vol.%) than the titanomagnetite population (15 vol.%) (Fig. 3e) (cf. Supplementary Data 3). The apparent decrease of phlogopite population density $<0.05 \mu\text{m}$ in crystal length may be representative of the occurrence of the Ostwald ripening^{20,51}. Also note that the line representative of the binodal droplet population (47 vol.%) is coherently above the titanomagnetite one (i.e., titanomagnetites cannot be more voluminous than the binodal droplets).

The second identified texture has been specifically investigated in the inner lava rims of sample MAY01-DR0101. BSE-SEM images (Fig. 4a) show similar macro- and micro-textures as observed in the inner lava rims of the MAY02-DR080102 sample. The main difference is that the nanoscale binodal-type liquid immiscibility, which is observed near the microlites, rapidly develops into a quite different texture more distally. Raman spectra performed on the matrix (cf. Supplementary Data 2) also show similar signatures as shown in area 2, Fig. 2d, confirming the presence of amorphous and/or crystalline nanoscale heterogeneities in this facies. Nevertheless, the acquired spectra show slight differences compared to the MAY02-DR080102 sample. The low-wavenumber peak at ca. 75 cm^{-1} , interpreted as the occurrence of the Boson peak, is identifiable and suffers slightly less from interference with secondary peaks compared to the MAY02-DR080102 sample. The observed peak between 600 and 700 cm^{-1} is also more diffuse than in the inner lava rims of the MAY02-DR080102 sample, suggesting that Fe-bearing nanolites are much less abundant than in the binodal-type texture. HAADF-STEM images (Fig. 4b) reveal that this texture is characterized by a nanoscale spinodal-type liquid immiscibility. In spinodal liquid immiscibility separation of the immiscible melts occurs spontaneously with no activation energy required but with kinetic limitations (i.e., it is thought to occur under high degrees of rapid undercooling⁵²). It is typically characterized by a highly inter-connected and deformed tube structure of two different melts¹, which contrasts with the expression of the nucleating and growing droplets of the binodal-type liquid immiscibility. The diameter/thickness of these spinodal tubes is ca. 50 nm. Both unmixed melt phases are associated with slight partial nanoscale crystallization. These nanolites tend to nucleate at the interface between the two melt phases and on synchronously formed nanolites that ultimately form elongated aggregates of nanolites (Fig. 4b). Reconstructed images from EDXS-STEM and EF-TEM (Fig. 4c) highlight that one melt phase is enriched in Ca, Fe, and Ti (with Fe- and Ti-rich nanolites) and the other is enriched in Si and Al (with Mg-rich nanolites), similarly to the binodal-type texture. BF-TEM, HR-TEM, and SAEDP data confirm that most of the spinodal texture is amorphous, but with the same mineralogy as in the binodal-type texture (Fig. 4d). Indeed, CSD data (Fig. 4e) show that nanolites are much less developed (5 vol.% of titanomagnetites and 1 vol.% of phlogopites) but slightly larger (maximum length of $0.3 \mu\text{m}$) than in the binodal-type texture (cf. Supplementary Data 3).

Most importantly, binodal-type and spinodal-type textures are not specific to the inner lava rims of the MAY02-DR080102 and MAY01-DR0101 samples, respectively. In fact, these two textures occur ubiquitously in all observed inner lava rims (cf. Supplementary File 1) but are not randomly distributed: binodal areas are preferentially observed around the quenching microlites (i.e., mostly acicular laths of biotite-formed during the lava quenching), while spinodal areas tend to preferentially develop in zones beyond the binodal areas.

As a summary, this case, characterized by both binodal- and spinodal-type textures, demonstrates that eruptive melts from Fani Maoré eruption are not efficiently quenched (ca. $1\text{--}1000 \text{ }^\circ\text{C s}^{-1}$) in the inner lava rims (from ca. $500 \mu\text{m}$ to 1 cm deep from the lava margin). Quenching microlites are formed and nanoscale liquid immiscibility occurs in the background matrix, which induces fast nanolite crystallization before the remaining melts transform into glass.

Case 3: Classical crystallization induced by slow cooling in the lava interiors. Finally, BSE-SEM images acquired in the lava interiors from the MAY02-DR0801 sample (Fig. 5a) reveal a texture distinct from those identified in the outer and inner lava rims. In this sample area, the background matrix is no longer characterized by liquid immiscibility, but by a significant microscale to nanoscale crystallization. Raman spectra of the matrix (cf. Supplementary Data 2) show similar signatures as shown in area 3, Fig. 2d, confirming the occurrence of significant crystallization in these facies, including Fe-bearing phases. HAADF-STEM images (Fig. 5b), together with EDXS-STEM (Fig. 5c) and BF-TEM as well as SAEDP data (Fig. 5d) reveal the presence of euhedral to sub-euhedral clinopyroxenes, ilmenites, biotites, and apatites, in decreasing order of volumetric abundance. Associated CSD (Fig. 5e) highlights that the apatites are generally smaller (30 to 300 nm in length) but much more numerous (population density up to $7500 \mu\text{m}^{-4}$) than the other micrometer-scale phases (cf. Supplementary Data 3). The overall CSD concave trend observed in this sample also suggests that this crystallization was controlled by both nucleation (mostly apatites) and growth (mostly ilmenites, clinopyroxenes, and biotites), which is a typical signature of classical cooling at eruptive conditions⁵³.

In conclusion, this case, characterized by classical microlite and nanolite crystallization, demonstrates that eruptive melts from Fani Maoré eruption are slowly cooled down (ca. $<1 \text{ }^\circ\text{C s}^{-1}$) in the lava interior areas deeper than 1 cm from the lava margin. Note that from ca. 5 cm from the lava margin, lava interiors tend to be fully crystallized mainly because of crystal growth allowed by relatively slow cooling rates (ca. $0.1 \text{ }^\circ\text{C s}^{-1}$, Fig. 2b) (cf. Supplementary File 1).

Discussion

Magmatic liquid behavior upon different quenching/cooling rates. The three previously described cases show that the eruptive melt behaves differently upon different eruptive quenching/cooling rates (i.e., different undercooling rates).

- (1) When experiencing relatively fast quenching rates ($>ca. 1000 \text{ }^\circ\text{C s}^{-1}$, i.e., in the outer lava rims), the erupted homogeneous magmatic melt is quenched and transformed into glass in less than 1 s (cf. Supplementary Information S11), recording the pre-emission magma signatures (step 1 in Fig. 6a), with no time for post-eruptive crystallization, liquid immiscibility, or degassing, which could change the lava texture and geochemistry from its pre-eruptive state (i.e., this area is the most ideally preserved material that is representative of the initial eruptive melt without any major post-eruptive modification).

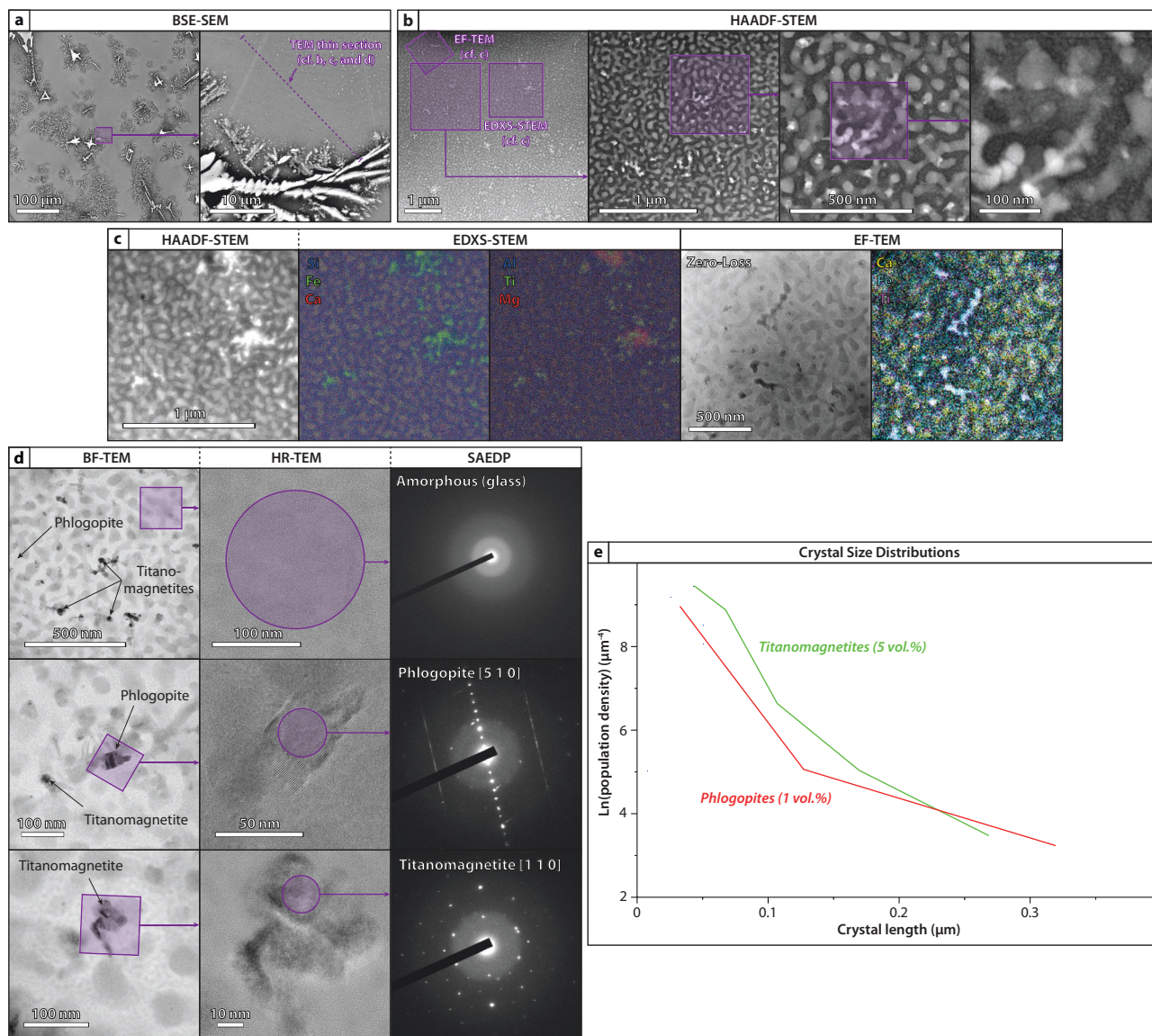


Fig. 4 Textural and chemical investigations made on the inner lava rim of the MAY01-DR0101 sample, representative of the spinodal-type texture. **a** BSE-SEM images. **b** HAADF-STEM images. **c** Reconstructed chemical maps from EDXS-STEM. **d** Sample mineralogy characterized by BF-TEM and HR-TEM, with associated SAEDP. **e** CSD analysis performed on the acquired HAADF-STEM images.

(2) When experiencing moderate quenching rates (between ca. 1 and 1000 °C s⁻¹, i.e., in the inner lava rims), the erupted magmatic melt exhibits a slight increase in melt differentiation (because of minor crystallization, i.e., microlites of biotite) and a decrease of temperature (because of natural lava cooling). As a result of these two changes, the residual magmatic melt falls into the liquid immiscibility field (step 2 in Fig. 6a). For this area, the cooling from the eruptive temperature down to the glass transition temperature range occurred between ca. 1 s (for a cooling rate of 1000 °C s⁻¹) and 8–10 min (for a cooling rate of 1 °C s⁻¹), which is enough time to enable crystallization and liquid immiscibility (cf. Supplementary Information S11). Interestingly, the fact that homogeneous glassy (case 1), binodal-type, and spinodal-type (case 2) textures are simultaneously observed within a narrow region of interest in the studied lavas (i.e., sometimes within less than a millimeter) suggests that the temperature vs. composition path experienced by the magmatic melt must be close to the so-called critical point, which represents the conditions where these three textures

can coexist¹ (Fig. 6a). Moreover, the fact that the volumetrically dominant melt phase is represented by the background matrix enriched in Si and Al, highlights that this quenching path is heading towards a similar theoretical melt composition, in agreement with the natural differentiation evolution of a magmatic melt¹ (step 2 in Fig. 6a). Note that this metastable liquid immiscibility, occurring in strong disequilibrium due to the involvement of high to moderate cooling rates, has to be considered to be distinct from the super- or sub-liquidus liquid immiscibility, which is considered to be in equilibrium and thermodynamically stable^{1,54}. Also note that the difference in liquid immiscibility textural type (binodal vs. spinodal) cannot be explained by a difference in undercooling as these textures are observed within relatively small areas in the Fani Maoré inner lava rims which surely experienced the same cooling histories. It is more likely a compositional effect of quenching microlite crystallization, which depletes the surrounding melt composition in certain elements, and by doing so ultimately changes the nature of the liquid

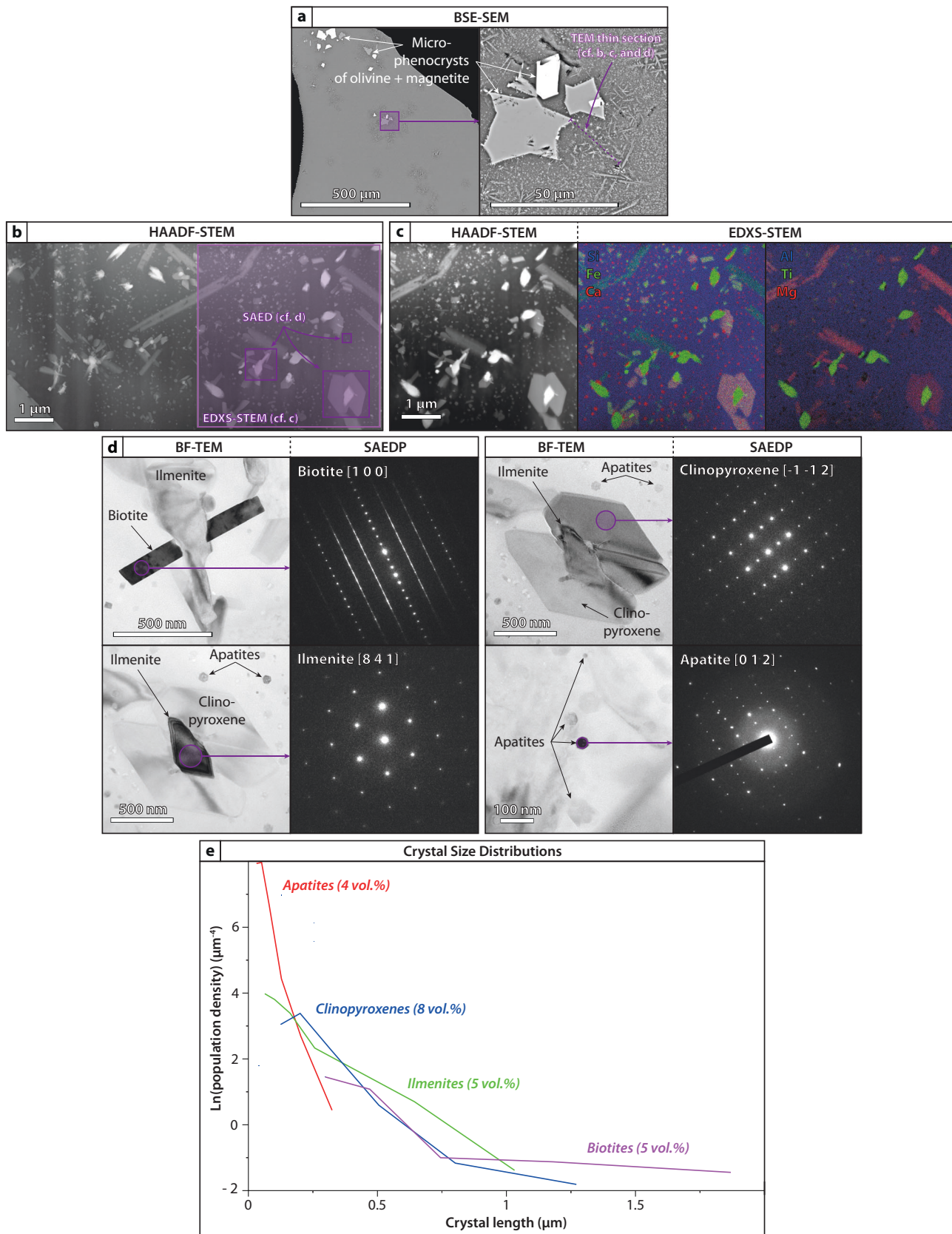


Fig. 5 Textural and chemical investigations made on the lava interior of the MAY02-DR0801 sample, representative of the classical crystallized texture. **a** BSE-SEM images. **b** HAADF-STEM images. **c** Reconstructed chemical maps from EDXS-STEM and EF-TEM. **d** Sample mineralogy characterized by BF-TEM and HR-TEM, with associated SAEDP. **e** CSD analysis performed on the acquired HAADF-STEM images.

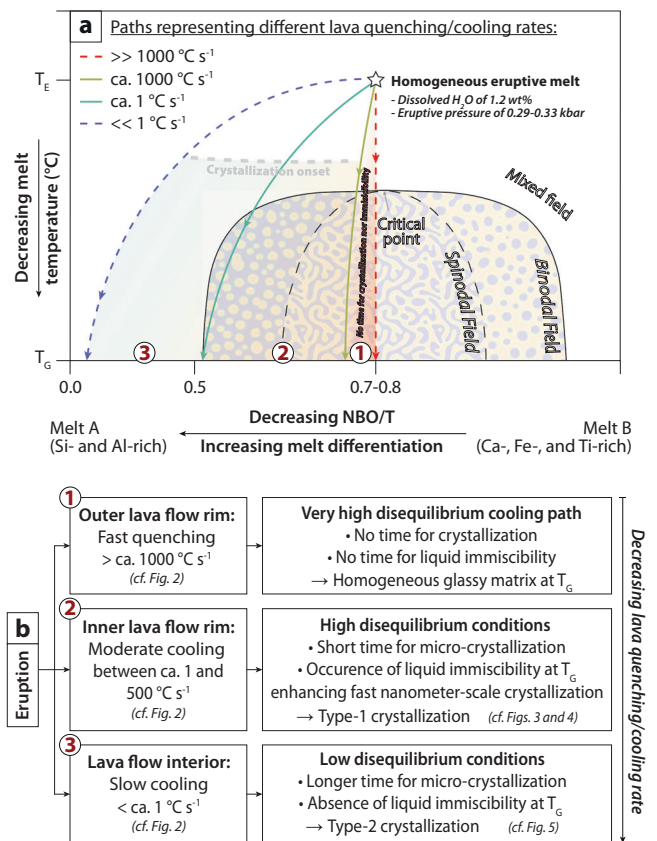


Fig. 6 Illustration of the origin of the studied lava flow textures. **a** Schematic representation of liquid immiscibility occurrence on a binary melt temperature-composition diagram (not to scale). T_E et T_G represent the eruptive temperature (ca. 1095 °C²⁹) and glass transition temperature range (between ca. 500 and 600 °C²⁷), respectively. Cases 1, 2, and 3 correspond to the different lava flow facies that are identified in Fig. 2 and independently investigated in Figs. 3, 4, and 5, respectively. **b** Summary of the processes involved in each lava facies.

immiscibility from spinodal to binodal around the newly formed microlites. This process has already been suggested in some Kilauea Iki lava lake samples, where binodal-type liquid immiscibility is triggered by compositional boundary layers around plagioclase microlites¹⁴. In our case, biotite (i.e., aluminosilicate) micro-crystallization must increase the Fe and Ti concentrations in the residual melt. The relatively low incompatibility of these two latter elements in the matrix can be considered as the main driving force of the formation of amorphous atomic clusters and then nanolites⁵⁰, which can be also accounted here as the origin of the homogeneous to spinodal and binodal transition, together with the low liquid-liquid interfacial energy that must facilitate the generation of emulsions¹⁵.

- (3) Finally, when experiencing relatively slow cooling rates (< ca. 1 °C s⁻¹, i.e., in the lava interiors), the relatively slow kinetics involved allow the erupted magmatic melt to be in slighter disequilibrium compared to the previous case. For this area, the cooling from the eruptive temperature down to the glass transition temperature range took more than 8–10 min (cf. Supplementary Information SI1), which is enough for pervasive crystallization. Lava interiors do not directly evidence the occurrence of liquid immiscibility (step 3 in Fig. 6a), even though immiscibility could have occurred and its signature might have been lost during further cooling. This is however unlikely as we observed

very different crystals between case 2 and case 3, in terms of both phase and texture. Note that at 5 cm of depth (i.e., where the lava tends to be fully crystallized), lava took ca. 1.4–1.7 h to cool down the glass transition temperature range (cf. Supplementary Information SI1).

Why does liquid immiscibility favor crystallization? By cooling a liquid below its liquidus temperature (e.g., quenching/cooling of a magmatic/volcanic melt during an eruption), it becomes a super-cooled liquid from which crystalline phases will tend to form⁵⁵. This phenomenon happens in two steps: (i) nucleation, which is the formation of atomic cluster/nucleus from the super-cooled liquid, and (ii) growth, which represents the nucleus size evolution to larger sizes after reaching the critical nucleus size. These two phenomena combined are called crystallization⁵⁶. The classical nucleation theory is still commonly used to describe crystal formation in silicate systems^{55,56}. This theory is based on a balance between thermodynamic and kinetic parameters and the steady-state crystal nucleation rate (I_{st} in m⁻³ s⁻¹) is given by:

$$I_{st} \sim CD \exp\left(\frac{-\alpha W_C}{k_B T}\right), \quad (1)$$

where C is a nearly constant value (in m⁻⁵), D is the effective diffusion coefficient of the structural unit of the melt phase (in m² s⁻¹), α is a dimensionless number linked to the crystal nucleation on pre-existing surfaces (ranging from 0 and 1), W_C is the critical work for nucleus formation (in J), k_B is the Boltzmann constant (in J K⁻¹), and T is the temperature of the system (in K). The effective diffusion coefficient (related to the viscosity by the Stokes-Einstein-Eyring relation) and the critical work for crystal formation are expressed respectively as:

$$D \sim \frac{k_B T}{\eta d_0}, \quad (2)$$

and

$$W_C = \frac{16\pi\sigma^3}{3\Delta G_V}, \quad (3)$$

where η is the viscosity of the melt phase (in Pa s), d_0 is an atomic parameter linked to the atomic jump distance (in m), $16\pi/3$ refers to the spherical radius of the forming crystalline phase, σ is the surface free energy (in J m⁻²), and ΔG_V is the thermodynamic driving force (in J m⁻³). When a silicate melt undergoes liquid immiscibility, the novel melt phases are separated by an interface and present different chemical compositions when compared to the initially mixed melt. Both factors may affect the aforementioned parameters for crystal nucleation and it will consequently alter crystallization¹⁵.

Firstly, it has been shown that for several systems undergoing liquid immiscibility, the novel melt phase compositions are often shifted towards that of a stoichiometric crystalline phase, which in turn enhances the thermodynamic driving force for nucleation (ΔG_V), and favors crystal nucleation¹⁵ (cf. Equation 1 and Eq. 3). In the investigated Fani Maoré inner lava rims, the matrix is separated into two melt phases, either in binodal- (Fig. 3) or spinodal-type (Fig. 4) textures. In each case, one melt phase is enriched in Fe, Ti, and Ca, which gives rise to nanolites enriched in Fe and Ti (titanomagnetites) with a residual Ca-rich melt composition. The other melt phase is enriched in Si and Al, leading to the crystallization of aluminosilicate nanolites (i.e., phlogopites).

Secondly, these compositional changes also induce the formation of an important viscosity contrast between the two melt phases, which are also different from the initially mixed melt viscosity⁴¹. The viscosity of silicates is closely linked to the

structural functions exerted by their compounds. The structural environment of Fe is complex since it may exist in two oxidation states (Fe^{3+} and Fe^{2+}) as well as in 4-, 5-, and 6-fold coordination⁵⁷. Titanium, in its turn, is generally presented on Earth as Ti^{4+} and can also have 4-, 5-, and 6-fold coordination⁵⁸. As a result, the silicate melt viscosity decreases when Fe and/or Ti are added to silicate networks^{59,60}. Moreover, this viscosity decrease is more pronounced at lower temperatures, where the entropic effect is more relevant⁶⁰. In this low-viscosity scenario, higher atomic mobility is reached and therefore, a higher nucleation rate is expected in these zones (see Eq. 1 and Eq. 2)¹⁵. Also, the Stokes-Einstein-Eyring relation (cf. Equation 2) provides a good approximation of atomic mobility in melts that undergo near-stoichiometric crystal nucleation at relatively high temperatures. This could explain why titanomagnetites are much more abundant in the melt phase enriched in Fe, Ti, and, Ca (since this latter element also lowers viscosity) than phlogopites in the melt phase enriched in Si and Al (which are elements working as a network formers increasing melt viscosity⁵⁸). It is also important to mention that a decoupling between viscosity and diffusion has been observed at deeper undercooling, which can also affect crystal growth, especially for systems undergoing nanoscale compositional reorganization and non-isochemical nucleation⁶¹.

Thirdly, two other parameters can enhance crystal nucleation at the interface between two melt phases. On the one hand, the crystal nucleation can occur directly on this new interface: this heterogeneous nucleation process decreases the alpha parameter of Eq. (1), and therefore increases the crystal nucleation rate. On the other hand, the enrichment of certain elements at the boundaries between the melt phases is generating a local zone with a higher driving force for nucleation and/or higher atomic mobility¹⁵. Despite the fact that nucleation facilitation at the droplet interface is not common in silicates due to the low interfacial energy of liquid droplet when compared to crystal/nucleus interfaces¹⁵, this type of heterogeneous nucleation is widely observed in our system (Figs. 3b and 4b). Also, note that this is not the first time that preferential nucleation of crystals at the droplet interface has been observed⁶². Since this interfacial energy is expressed per unit area (i.e., $\text{J}\cdot\text{m}^{-2}$) and in our case, we have nanoscale droplets, it is expected that the absolute amount of energy is much greater, and consequently a nucleation events will be favored at the interfaces. This explains why nanolites are more abundant in the binodal-type texture than in the spinodal-type one. It is also important to note that nanolite aggregation is enhanced in both binodal and spinodal-type textures but in different ways: binodal texture favors the formation of rounded aggregates of nanolites while spinodal texture favors the formation of chains of nanolites.

Finally, and in addition to the impact on the three aforementioned processes, it is important to emphasize that Fe- and Ti-bearing silicates generally present a worse glass-forming ability (i.e., the propensity of a melt to vitrify upon cooling), being, therefore, more prone to undergo crystallization than Fe- and Ti-poor silicates⁶³.

Conclusions and perspectives on the potential impacts of metastable liquid immiscibility in magmas. This study highlights that Fani Maoré magmas are subject to metastable liquid immiscibility at nanoscale and upon moderate quenching rates in the range of 1 to $1000\text{ }^\circ\text{C s}^{-1}$, likely to occur in numerous eruptive cases (e.g., submarine eruption of lavas and pyroclasts, but also post-eruptive cooling in air of lavas/pyroclasts, as well as syn-eruptive phreatomagmatic interactions). This process is associated with an enhanced nanoscale crystallization, producing

nanoscale mineralogy (i.e., nanolite chemical compositions) and textures (i.e., CSDs, crystal habits and shapes, and occurrence of aggregation) that are significantly different from the classical nanoscale crystallization originating from a homogeneous mixed volcanic melt (Fig. 6b). Therefore, this study highlights a new mechanism for nanolite generation in unmixed volcanic melts and opens up new questions about its potential impacts on the physicochemical characteristics of magmas, and at the end, on volcanic phenomena, given that nanolites are claimed to impact key processes of eruptive dynamics such as (i) volatile degassing and (ii) magma viscosity^{17–21,23–26,50}.

(i) Liquid immiscibility and associated crystallization likely significantly affect the degassing behavior of the volatile species dissolved in the magmatic melts (e.g., H_2O , CO_2 , SO_2 , F, and Cl). Based on the observed physicochemical characteristics of the inner lava rims of Fani Maoré lavas (this study) and on previously performed Simultaneous Thermal Analysis and Evolved Gas Analysis (STA-EGA) experiments on the same samples²⁷, a complex magmatic volatile segregation emerges. First, the crystallization of hydrated minerals (i.e., biotites and phlogopites) is impacted by the initial dissolved H_2O content⁶⁴, and at the end must control volatile concentrations of the residual melts. Second, we speculate that H_2O , F, and Cl tend to migrate in the Si- and Al-rich melt, as phlogopite nanolites, which ideally contain the aforementioned volatile species, are only observed within this melt. During STA-EGA experiments, the main part of H_2O (0.8–1 wt.%) is degassed just above T_G upon heating and corresponds to the H_2O mainly dissolved in the residual Si- and Al-rich melt, while a small amount of H_2O (0.2–0.3 wt.%) is degassed synchronously to endothermic crystal melting and corresponds to the H_2O stored within the biotites and phlogopites. This volatile degassing behavior for unmixed systems highly contrasts with samples implying homogeneous residual melts, which only show one degassing step originating from the mixed melt²⁷. Note that the relatively high eruptive pressures involved in the Fani Maoré eruption (0.29–0.33 kbar) led to a relatively high H_2O dissolved content (1.2 wt.% because of the high H_2O solubility as a function of pressure) compared to low SO_2 (initially low content in the parental magma) and CO_2 (mainly exsolved forming CO_2 -rich vesicles because of the low CO_2 solubility as a function of pressure) contents²⁷. Also, note that crystals with high contact angle values between bubbles and the surrounding melt (i.e., high wettability), exhibit textures reflecting strong bubble-particle interaction, which alter bubble dynamics and outgassing regimes of multiphase systems⁶⁵. Therefore, in a scenario involving relatively lower eruptive pressures than the ones of Fani Maoré, heterogeneous nucleation of bubbles is expected to be strong on the titanomagnetite nanolites, which have a relatively high wettability and which densely form at the liquid-liquid interface between the two unmixed melts, therefore enhancing bubble generation in contact with these nanolites, preferentially within the Si- and Al-rich melt⁶⁶.

(ii) In the presence of these nanoscale phases, magma viscosity is also expected to increase due to chemical modifications of the remaining silicate melts and because of the physical presence of suspended crystals^{20,22–24}. Since nanolites are generally Si-poor crystals, there must be an increase of the Si content within the remaining melt composition, and therefore an increase of viscosity^{23,67}. In our case, this Si increase already occurred at the melt unmixing stage when the Fe- and Ti-rich melt was formed. It has been also shown for analog materials that the physical presence of nanolites increase the viscosity of the system, especially for low rates of shear (e.g., Brownian regimes). If these scenarios are achieved in conditions suitable for volcanic systems, particle aggregation is facilitated and during this process, particles

trap fluid in the aggregate interstices, increasing the apparent volume fraction of crystals (by the creation of dead-fluid volumes), and therefore inducing a viscosity increase²². Finally, it should be noted that the viscosity of the unmixed system will be also impacted due to the distribution of volatile contents, as some volatiles are known to impact melt viscosity⁶⁷.

In conclusion, if nanoscale metastable liquid immiscibility and associated crystallization are indeed moving toward more (i) porous and (ii) viscous magmas, this newly evidenced mechanism could most likely enhance primary magma fragmentation, but also secondary fragmentation of cooling lavas and/or pyroclasts⁶⁸. Indeed, the potential increase of magma porosity (still with a low permeability because of the generation of isolated bubbles on the nanolites), and the potential increase of magma viscosity would drastically decrease the magma fragmentation threshold (by decreasing the glass transition temperature range and the strain rate needed to fragment the magma^{68,69}). All these processes are identified as key points for eruptive dynamics in volcanology (i.e., directly linked to the generation of different hazards and related risks). Also, a possible influence of the redox state evolution on the liquid immiscibility occurrence and crystallization path should be better investigated, as quenching/cooling rates might influence iron speciation and liquidus temperatures of the melts. For these reasons, the description of such metastable liquid immiscibility and associated nanolite crystallization upon eruption deserves further investigation in order to decipher under which conditions (i.e., magma composition, pressure, and temperature evolutions) this kind of texture can develop naturally, and experimentally measure its specific effect on volatile degassing as well as on rheology, under relevant volcanic conditions.

Methods

Lava sampling and selection. Investigated rock samples were dredged during MAYOBS01³⁶, MAYOBS02³⁷, and MAYOBS15³⁸ oceanographic campaigns (operated by the Marion Dufresne II research vessel). A cylindrical metallic dredge with cutting teeth was used in order to break off samples from their original submarine outcrops³¹. Each dredge was remotely pulled by a cable along the ocean floor and could collect a maximum of ca. 1000 kg of sample from which a first selection of clasts from fresh lava flow margins was performed onboard. Then, a second selection was realized in the laboratory to pick up the best-preserved samples for further analysis, as described hereafter. All samples were collected and exported in a responsible manner and in accordance with relevant permits and local laws.

Lava quenching/cooling rates estimation by heat transfer calculations. When an idealized planar geometry that has a plane surface and extends to infinity in all directions except one undergoes a sudden change in temperature on one of its sides (i.e., applicable to lava flows), transient one-dimensional conduction will occur within this material. An energy balance is developed based on an infinitesimal element of volume inside the body that is exchanging energy:

$$[\text{heat input rate}] - [\text{heat output rate}] + [\text{heat generation rate}] = [\text{heat rate accumulation}] \quad (4)$$

By applying this relation to a cartesian system and considering the material properties in the three orthogonal components (x , y , z) that have the same thermal properties (isotropic material), one

can obtain the following expression for the energy balance:

$$\alpha \left(\frac{\partial^2 T}{\partial x^2} + \frac{\partial^2 T}{\partial y^2} + \frac{\partial^2 T}{\partial z^2} \right) + \frac{\dot{q}}{\rho C_p} = \frac{\partial T}{\partial t}, \quad (5)$$

$$\alpha = \frac{\kappa}{\rho C_p}, \quad (6)$$

where α is the thermal diffusivity ($5.0 \cdot 10^{-7} \text{ m}^2 \text{ s}^{-1}$ (ref. ⁷⁰)) that is defined in Eq. (6), T is the temperature at a given time t , \dot{q} is the rate of energy generation per unit of volume, ρ is the density (of the basanitic liquid 2700 kg m^{-3} (ref. ²⁹), also coherent with the density used in ref. ⁷⁰), C_p is the specific heat capacity ($1259 \text{ J kg}^{-1} \text{ K}^{-1}$, deduced from Eq. (6), also coherent with values from⁷¹), and κ is the thermal conductivity ($1.7 \text{ W m}^{-1} \text{ K}^{-1}$ (ref. ⁷⁰) of the magmatic melt. For our specific case, it can be considered that (i) the lava flow morphology has two dimensions much larger than the third one (planar geometry), and (ii) that the generation of heat (i.e., latent heat of crystallization) is minor and can be neglected. This latter assumption is based on Differential Scanning Calorimetry (DSC) measurements on the Fani Maoré lava samples in order to measure the exothermic heat related to the sample crystallization, which only represents 5.3% of the total heat absorption by seawater that is estimated in parallel by theoretical calculations (cf. Supplementary Information SI1). Also note that due to the hydrostatic pressure exerted on the erupted lavas (i.e., eruptive pressure of 0.29–0.33 kbar), bubble formation is mostly hindered²⁷ (i.e., sample average porosity of 35 vol%, large vesicles being mostly found in the internal parts of the lavas) and therefore these thermal calculations in the absence of significant bubble fraction is still valid. Thus, Eq. (5) becomes:

$$\alpha \left(\frac{\partial^2 T}{\partial x^2} \right) = \frac{\partial T}{\partial t} \quad (7)$$

If a sudden change of conditions is imposed at the body's surface (e.g., interaction with colder seawater), transient and one-dimensional conduction will take place within the solid. In this case, two conditions are applied to solve the problem (i) at the initial moment, the whole solid has a constant temperature in all points equals to the eruptive temperature and (ii) the surface temperature for any time greater than zero has the surface temperature constant and equal to the external temperature. Therefore, the analytical solution considering Eq. (7) and the aforementioned conditions is given by the semi-infinite approach solution:

$$\frac{T - T_E}{T_{SW} - T_E} = \text{erf} \left(\frac{x}{2\sqrt{\alpha t}} \right), \quad (8)$$

where T is the local temperature of lava (in °C) at a given depth from the rim x (in m), T_E is the initial eruptive temperature of lava (1095 °C ²⁹), T_{SW} is the seawater temperature (considered as 10 °C), and t is the time the lava takes to cool from T_E to T (in s). Two different final temperatures of 500 and 600 °C (cf. blue and red lines in Fig. 2b) were considered for T when executing the calculations. These temperatures correspond to the expected glass transition (T_G) temperature range of these magmatic melts²⁷ (cf. also Supplementary Information SI1) below which any physical change, such as crystallization, is disregarded. Note that taking either T_G value, the obtained quenching rates are similar.

Sample preparation for inductively coupled plasma atomic emission spectroscopy (ICP-AES), Raman spectroscopy, and scanning electron microscopy (SEM) analyses. The selected samples were dried for 72 h at 60 °C . Then, they were manually broken into coarse chips ($\leq 1 \text{ cm}$). One part of these chips was

subsequently powdered with an agate mortar to perform an ICP-AES analysis. The other part of the rock chips was used to make impregnated-epoxy polished sections for Raman and SEM analyses. For SEM analyses, polished sections were carbon coated (10 nm) using a Leica Sputter Coater EM ACE600.

Bulk rock composition acquired by ICP-AES. Powdered samples were mixed with LiBO_2 , placed in a graphite crucible, and melted in an induction oven at 1050 °C for 5 min, resulting in homogeneous glasses. Each of these glasses was dissolved in a solution of deionized H_2O and HNO_3 , and finally diluted by a factor of 2000. The final solutions were analyzed using an Agilent 5800 VDV ICP-AES, following an already documented procedure⁷², giving an external reproducibility (2σ error) between 1 and 3% for all major elements, except for K_2O , MnO (4%), and P_2O_5 (7%), calibrated on the DR-N standard (diorite). Note that compositions of samples from MAYOBS01 and MAYOBS02 are already published²⁹, following the same procedure.

Groundmass signature investigated by Raman spectroscopy. Raman spectra were acquired on the sample groundmass from 50 to 1300 cm^{-1} Raman shift, using a Jobin Yvon XPlora One spectrometer coupled with an Olympus microscope, adapted from an already documented procedure⁴⁹. The instrument was calibrated using a silicon standard. Instrumental settings consisted of 1800 grooves/mm grating density, a confocal hole of 300 μm , and a slit of 200 μm with an exposure time of 10 s repeated 3 times. A $\times 100$ magnification was used during the acquisitions, with a laser excitation wavelength of 532 nm and an applied filter of 50%. Preliminary acquisition tests have been performed from 50 to 100 cm^{-1} Raman shift on pure glasses and crystals to confirm the application of this procedure also on low-wavenumber region, with a 532 nm edge filter. Raman spectra were systematically collected near the sample surfaces (from 0 to ca. 3 μm of depth), in order to get intense enough signals and at the same time check the analyzed textures with the microscope. All qualitative Raman analysis can be found in Supplementary Data 2.

Microscopic texture investigated by SEM. Back-Scattered-Electron images acquired by SEM (BSE-SEM) were done using a Hitachi SU5000 Field-Emission SEM with a high vacuum-mode and an acceleration voltage of 10 kV. All BSE-SEM images acquired for this project can be found in Supplementary Information SI2 and Supplementary File 1.

Sample preparation for transmission electron microscopy (TEM). Thin sections for TEM analyses were systematically made perpendicular to the sample surface imaged by BSE-SEM, following the thin section lift-out technique that uses a FEI Strata DB235 Focused Ion Beam Scanning Electron Microscope (FIB-SEM), allowing a high spatial precision, which is good enough to isolate specific region of interest for detailed TEM analyses. TEM preparation and lift out were performed at 30 kV with the intensity of 7 nA to 100pA and a final cleaning at 5 kV to limit amorphization. SEM images related to the TEM thin sections can be found in Supplementary Information SI3.

Nanoscale texture and chemistry investigated by TEM. TEM observations were carried out using a Jeol 2100F TEM with a Schottky emitter operating at 200 kV, equipped with a high-resolution pole piece, a Gatan US4000 CCD camera, a Gatan GIF 2001 electron energy loss spectrometer, and a Jeol Si(Li) X-ray energy-dispersive spectrometer. TEM analysis consisted of different techniques. (i) The use of a high-angle annular dark field detector in the scanning transmission electron microscopy mode

(HAADF-STEM) provided sample images based on the atomic number (Z contrast), similar to BSE-SEM images. Electrons were collected at high angles in the range of 60–170 mrad. Chemical mapping using (ii) Energy-dispersive X-ray spectroscopy acquired by STEM (EDXS-STEM) and (iii) Energy-filtered TEM (EF-TEM) was realized to infer the spatial distributions of chemical elements. (iii) Bright field and (iv) High-resolution images acquired by TEM (BF-TEM and HR-TEM) as well as associated (v) Selected area electron diffraction patterns (SAEDP) were acquired to identify the different crystalline phases occurring in the selected samples. Mineralogical identification based on SAEDP was performed using the single crystal software. For small crystals unsuitable for SAEDP analysis, fast Fourier transforms (FFT) were directly realized from the HR-TEM images to produce diffraction patterns.

Crystal size distribution (CSD) analysis. CSD analysis was performed following an already described procedure⁷³. Binarized images used for the analysis were created both from HAADF-STEM and EDXS-STEM images. For CSD calculations using CSDcorrections software, the 3-dimensional crystal habits of each phase were estimated using the CSDslice database⁷⁴. Images and CSD data can be found in Supplementary Data 3.

Data availability

All data used in this paper are available in the supplementary material of this paper, also published in the EarthChem public repository data (<https://doi.org/10.60520/IEDA/113054>), and available on request to the corresponding author.

Received: 26 April 2023; Accepted: 4 December 2023;

Published online: 16 December 2023

References

- Schuller, S. in *From Glass to Crystal: Nucleation, Growth and Phase Separation: From Research to Applications*. 125–154 (EDP Sciences, 2017).
- Greig, J. W. Immiscibility in silicate melts; part I. *Am. J. Sci.* **5**, 1–44 (1927).
- Freestone, I. C. Liquid immiscibility in alkali-rich magmas. *Chem. Geol.* **23**, 115–123 (1978).
- Philpotts, A. R. Silicate liquid immiscibility in tholeiitic basalts. *J. Petrol.* **20**, 99–118 (1979).
- Bogaerts, M. & Schmidt, M. W. Experiments on silicate melt immiscibility in the system Fe_2SiO_4 - KAlSi_3O_8 - SiO_2 - CaO - MgO - TiO_2 - P_2O_5 and implications for natural magmas. *Contrib. Mineral. Petrol.* **152**, 257–274 (2006).
- Thompson, A. B., Aerts, M. & Hack, A. C. Liquid immiscibility in silicate melts and related systems. *Rev. Mineral. Geochem.* **65**, 99–127 (2007).
- Honour, V. C., Holness, M. B., Partridge, J. L. & Charlier, B. Microstructural evolution of silicate immiscible liquids in ferrobasalts. *Contrib. Mineral. Petrol.* **174**, 1–24 (2019).
- Panina, L. I. & Motorina, I. V. Liquid immiscibility in deep-seated magmas and the generation of carbonatite melts. *Geochem. Int.* **46**, 448–464 (2008).
- Veksler, I. V. Liquid immiscibility and its role at the magmatic-hydrothermal transition: a summary of experimental studies. *Chem. Geol.* **210**, 7–31 (2004).
- Veksler, I. V., Dorfman, A. M., Borisov, A. A., Wirth, R. & Dingwell, D. B. Liquid immiscibility and the evolution of basaltic magma. *J. Petrol.* **48**, 2187–2210 (2007).
- Charlier, B. et al. Large-scale silicate liquid immiscibility during differentiation of tholeiitic basalt to granite and the origin of the Daly gap. *Geology* **39**, 907–910 (2011).
- Philpotts, A. R. Compositions of immiscible liquids in volcanic rocks. *Contrib. Mineral. Petrol.* **80**, 201–218 (1982).
- Honour, V. C., Holness, M. B. & Stock, M. J. The effect of cooling rate on immiscible silicate liquid microstructure: an example from the Palaeogene dykes of Northeast England. *Mineral. Magaz.* **83**, 809–820 (2019).
- Honour, V. C. et al. Compositional boundary layers trigger liquid unmixing in a basaltic crystal mush. *Nat. Commun.* **10**, 1–8 (2019).
- Zanotto, E. D. Effect of liquid phase separation on crystal nucleation in glass-formers. Case closed. *Ceram. Int.* **46**, 24779–24791 (2020).

16. Sharp, T. G., Stevenson, R. J. & Dingwell, D. B. Microlites and nanolites in rhyolitic glass: microstructural and chemical characterization. *Bull. Volcanol.* **57**, 631–640 (1996).
17. Mujin, M. & Nakamura, M. A nanolite record of eruption style transition. *Geology* **42**, 611–614 (2014).
18. Matsumoto, K. & Geshi, N. Shallow crystallization of eruptive magma inferred from volcanic ash microtextures: a case study of the 2018 eruption of Shinmoedake volcano, Japan. *Bull. Volcanol.* **83**, 1–14 (2021).
19. Mujin, M., Nakamura, M. & Miyake, A. Eruption style and crystal size distributions: Crystallization of groundmass nanolites in the 2011 Shinmoedake eruption. *Am. Mineral.* **102**, 2367–2380 (2017).
20. Di Genova, D. et al. In situ observation of nanolite growth in volcanic melt: a driving force for explosive eruptions. *Sci. Adv.* **6**, eabb0413 (2020).
21. Cáceres, F. et al. From melt to crystals: the effects of cooling on FeTi oxide nanolites crystallisation and melt polymerisation at oxidising conditions. *Chem. Geol.* **563**, 120057 (2021).
22. Pereira, L., Vasseur, J., Wadsworth, F. B., Trixler, F. & Dingwell, D. B. Interparticle and Brownian forces controlling particle aggregation and rheology of silicate melts containing platinum-group element particles. *Sci. Rep.* **12**, 1–10 (2022).
23. Okumura, S. et al. Rheology of nanocrystal-bearing andesite magma and its roles in explosive volcanism. *Commun. Earth Environ.* **3**, 1–7 (2022).
24. Di Genova, D., Zandona, A. & Deubener, J. Unravelling the effect of nano-heterogeneity on the viscosity of silicate melts: Implications for glass manufacturing and volcanic eruptions. *J. Non-Cryst. Solids* **545**, 120248 (2020).
25. Cáceres, F. et al. Can nanolites enhance eruption explosivity? *Geology* **48**, 997–1001 (2020).
26. Knafelc, J. et al. Havre 2012 pink pumice is evidence of a short-lived, deep-sea, magnetite nanolite-driven explosive eruption. *Commun. Earth Environ.* **3**, 1–11 (2022).
27. Thivet, S., et al. Volatiles of the active Mayotte volcanic chain: STA & EGA-MS analysis of volcanic products. *Chem. Geol.* 121297. <https://doi.org/10.1016/j.chemgeo.2022.121297> (2023)
28. REVOSIMA. *Bulletin de l'activité Sismo-volcanique à Mayotte, Août, IGP, Université de Paris, OVPF, BRGM, Ifremer, REVOSIMA News-Institut de Physique du Globe de Paris (ipgp.fr)* (2022)
29. Berthod, C. et al. The 2018-ongoing Mayotte submarine eruption: Magma migration imaged by petrological monitoring. *Earth Planet. Sci. Lett.* **571**, 117085 (2021).
30. Feuillet, N. et al. Birth of a large volcanic edifice offshore Mayotte via lithosphere-scale dyke intrusion. *Nat. Geosci.* **14**, 787–795 (2021).
31. Berthod, C. et al. Temporal magmatic evolution of the Fani Maoré submarine eruption 50 km east of Mayotte revealed by in situ sampling and petrological monitoring. *Comptes Rendus. Géosci.* **354**, 1–29 (2022).
32. Berthod, C. et al. Mantle xenolith-bearing phonolites and basanites feed the active volcanic ridge of Mayotte (Comoros archipelago, SW Indian Ocean). *Contrib. Mineral. Petrol.* **176**, 1–24 (2021).
33. Foix, O. et al. Offshore Mayotte volcanic plumbing revealed by local passive tomography. *J. Volcanol. Geotherm. Res.* **420**, 107395 (2021).
34. Lavayssière, A. et al. A new 1D velocity model and absolute locations image the Mayotte seismo-volcanic region. *J. Volcanol. Geotherm. Res.* **421**, 107440, <https://doi.org/10.1016/j.jvolgeores.2021.107440> (2022).
35. Andújar, J. et al. Experimental evidence for the shallow production of phonolitic magmas at Mayotte. *Comptes Rendus. Géosci.* **354**, 1–32 (2022).
36. Feuillet, N. MAYOBS1 cruise. RV Marion Dufresne. <https://doi.org/10.17600/18001217> (2019)
37. Jorry, S. J. MAYOBS2 cruise. RV Marion Dufresne. <https://doi.org/10.17600/18001222> (2019)
38. Rinnert, E., Thinon, I., & Feuillet, N. MAYOBS15 cruise. RV Marion Dufresne. <https://doi.org/10.17600/18001745> (2020)
39. Mysen, B. O., Virgo, D. & Seifert, F. A. The structure of silicate melts: implications for chemical and physical properties of natural magma. *Rev. Geophys.* **20**, 353–383 (1982).
40. Middlemost, E. A. Iron oxidation ratios, norms and the classification of volcanic rocks. *Chem. Geol.* **77**, 19–26 (1989).
41. Verdum, P. et al. Viscosity of crystal-free silicate melts from the active submarine volcanic chain of Mayotte. *Chem. Geol.* <https://doi.org/10.1016/j.chemgeo.2023.121326> (2023)
42. Incropera, F. P., DeWitt, D. P., Bergman & T. L., Lavine, A. S. Introduction to heat transfer. 6th edn. John Wiley & Sons (2007).
43. Potuzak, M., Nichols, A. R., Dingwell, D. B. & Clague, D. A. Hyperquenched volcanic glass from Loihi seamount, Hawaii. *Earth Planet. Sci. Lett.* **270**, 54–62 (2008).
44. Mastin, L. G. Generation of fine hydromagmatic ash by growth and disintegration of glassy rinds. *J. Geophys. Res. Solid Earth.* **112**. <https://doi.org/10.1029/2005JB003883> (2007).
45. Heide, K., Woermann, E. & Ulmer, G. Volatiles in pillows of the Mid-Ocean-Ridge-Basalt (MORB) and vitreous basaltic rims. *Geochemistry* **68**, 353–368 (2008).
46. Cassetta, M., et al. Estimating the viscosity of volcanic melts from the vibrational properties of their parental glasses. *Sci. Rep.* **11**. <https://doi.org/10.1038/s41598-021-92407-5> (2021).
47. Malinovsky, V. K. & Sokolov, A. P. The nature of boson peak in Raman scattering in glasses. *Solid State Commun.* **57**, 757–761 (1986).
48. Takahashi, Y., Osada, M., Masai, H. & Fujiwara, T. Crystallization and nanometric heterogeneity in glass: In situ observation of the boson peak during crystallization. *Phys. Rev.B* **79**, 214204 (2009).
49. Di Genova, D. et al. Effect of iron and nanolites on Raman spectra of volcanic glasses: a reassessment of existing strategies to estimate the water content. *Chem. Geol.* **475**, 76–86 (2017).
50. Scarani, A. et al. A chemical threshold controls nanocrystallization and degassing behaviour in basalt magmas. *Commun. Earth Environ.* **3**, 1–14 (2022).
51. Voorhees, P. W. The theory of Ostwald ripening. *J. Stat. Phys.* **38**, 231–252 (1985).
52. Cahn, J. W. On spinodal decomposition. *Acta Metallurgica* **9**, 795–801 (1961).
53. Thivet, S. et al. Evidences of plug pressurization enhancing magma fragmentation during the September 2016 basaltic eruption at Piton de la Fournaise (La Réunion Island, France). *Geochem. Geophys. Geosyst.* **21**, e2019GC008611 (2020).
54. Veksler, I. V., Dorfman, A. M., Borisov, A. A., Wirth, R. & Dingwell, D. B. Liquid immiscibility and evolution of basaltic magma: reply to SA Morse, AR McBirney and AR Philpotts. *J. Petrol.* **49**, 2177–2186 (2008).
55. Cormier, L. Nucleation in glasses—new experimental findings and recent theories. *Procedia Mater. Sci.* **7**, 60–71 (2014).
56. Montazerian, M. & Zanotto, E. D. Nucleation, growth, and crystallization in oxide glass-formers. A current perspective. *Rev. Mineral. Geochem.* **87**, 405–429 (2022).
57. Henderson, G. S. & Stebbins, J. F. The short-range order (SRO) and structure. *Rev. Mineral. Geochem.* **87**, 1–53 (2022).
58. Farges, F. & Brown, G. E. Coordination chemistry of titanium (IV) in silicate glasses and melts. IV. XANES studies of synthetic and natural volcanic glasses and tektites at ambient temperature and pressure. *Geochim. Cosmochim. Acta* **61**, 1863–1870 (1997).
59. Dingwell, D. B. Shear viscosity of alkali and alkaline earth titanium silicate liquids. *Am. Mineral.* **77**, 270–274 (1992).
60. Chevrel, M. O., Giordano, D., Potuzak, M., Courtial, P. & Dingwell, D. B. Physical properties of CaAl₂Si₂O₈-CaMgSi₂O₆-FeO-Fe₂O₃ melts: analogues for extra-terrestrial basalt. *Chem. Geol.* **346**, 93–105 (2013).
61. Schmelzer, J. W. P., Abyzov, A. S., Fokin, V. M., Schick, C. & Zanotto, E. D. Crystallization in glass-forming liquids: effects of decoupling of diffusion and viscosity on crystal growth. *J. Non-Cryst. Solids* **429**, 45–53 (2015).
62. Ohlberg, S. M., Golob, H. R., & Strichler, D. Crystal nucleation by glass in glass separation. In: *Proceedings of the Symposium on Nucleation and Crystallization in Glasses and Melts, Columbus, Ohio, United States*. 55–62. (Columbus, 1962).
63. Cormier, L., Galois, L., Lelong, G. & Calas, G. From nanoscale heterogeneities to nanolites: cation clustering in glasses. *Comptes Rendus. Physique* **24**, 1–15 (2023).
64. Davis, M. J., Ihinger, P. D. & Lasaga, A. C. Influence of water on nucleation kinetics in silicate melt. *J. Non-Cryst. Solids* **219**, 62–69 (1997).
65. Pereira, L. et al. The physics of dancing peanuts in beer. *R. Soc. Open Sci.* **10**, 230376 (2023).
66. Gardner, J. E. et al. Bubble formation in magma. *Ann. Rev. Earth Planet. Sci.* **51**, 131–154 (2023).
67. Giordano, D., Russell, J. K. & Dingwell, D. B. Viscosity of magmatic liquids: a model. *Earth Planet. Sci. Lett.* **271**, 123–134 (2008).
68. Scheu, B. & Dingwell, D. B. Magma fragmentation. *Rev. Mineral. Geochem.* **87**, 767–800 (2022).
69. Colombier, M. et al. Degassing and gas percolation in basaltic magmas. *Earth Planet. Sci. Lett.* **573**, 117134 (2021).
70. Whittington, A. G., Hofmeister, A. M. & Nabelek, P. I. Temperature-dependent thermal diffusivity of the Earth's crust and implications for magmatism. *Nature* **458**, 319–321 (2009).
71. Leshar, C. E., & Spera, F. J. Thermodynamic and transport properties of silicate melts and magma. in *The encyclopedia of volcanoes* 113–141 (Academic Press, 2015).
72. Gurioli, L. et al. Integrating field, textural, and geochemical monitoring to track eruption triggers and dynamics: a case study from Piton de la Fournaise. *Solid Earth* **9**, 431–455 (2018).
73. Thivet, S., Gurioli, L. & Di Muro, A. Basaltic dyke eruptions at Piton de la Fournaise: characterization of the eruptive products with implications for reservoir conditions, conduit processes and eruptive dynamics. *Contrib. Mineral. Petrol.* **175**, 1–24 (2020).

74. Higgins, M. D. Measurement of crystal size distributions. *Am. Mineral.* **85**, 1105–1116 (2000).

Acknowledgements

This work has been supported by the Alexander von Humboldt Foundation, the ERC 2018 ADV Grant 834225 (EAVESDROP), the LMU Excellence PostDoc Support Fund, the Services d'Observation en Volcanologie (SNOV, INSU), and the Réseau de Surveillance Volcanologique et Sismologique de Mayotte (REVOSIMA), a partnership between IPGP, BRGM, OVPF-IPGP, CNRS, and IFREMER. The studied samples were collected by the MAYOBS set of campaigns that are authorized to collect geological samples in the area (<https://doi.org/10.18142/291>). MAYOBS1 campaign was funded by the CNRS-INSU TELLUS MAYOTTE program (SISMAYOTTE project). MAYOBS1 (mission chief: N. Feuillet; scientists onboard: C. Deplus, P. Bachelery), MAYOBS2 (mission chief: S. Jorry; scientist onboard: A. Le Friant, M. Bickert), and MAYOBS15 (mission chiefs: E. Rinnert, I. Thinon, N. Feuillet; scientist onboard: C. Berthod, J.-C. Komorowski) campaigns were funded by several French research institutions and laboratories (IPGP, CNRS, BRGM, IFREMER, IPGS). We also thank the captains and crews of the R/V Marion Dufresne (TAAF, IFREMER, LDA). Since June 2019, all REVOSIMA activities on Mayotte are funded by several French ministries (MESRI, MTE, MOM, MI, MA), with the support of DIRMOM and MAPPPROM. We thank A. Peltier (OVPF-IPGP) and C. Mucig (BRGM) respectively the Operational Leader and the Co-leader of the REVOSIMA. We are grateful to C. Cimarelli, M. Kaliwoda, D. Müller (LMU), C. Constantin and E. Chaudron-Vrignaud (LMV) for their assistance with SEM, Raman, EPMA, sample preparation and ICP-AES analysis, respectively. We also thank A. Di Muro (LGL-TPE) and P. Besson (IPGP) for constructive discussions, as well as the three anonymous reviewers, whose comments improved the quality of the manuscript. This study contributes to IdEx Université de Paris ANR-18-IDEX-0001.

Author contributions

S.T. and L.P. initiated the project. E.M., C.B., and J.-C.K. provided the samples. E.M. and C.B. provided the bulk rock compositions of the samples. S.T., L.P., K.-U.H. conceptualized and performed the heat transfer calculations, performed the sample preparation and analysis at the SEM and Raman. D.T. performed the sample preparation for the TEM. S.T. and N.M. carried out the TEM analysis and associated data treatment. S.T., L.P., E.M., P.V., C.B., D.B.D., and J.-C.K. participated in the data interpretation. S.T. wrote the majority of the paper. All authors reviewed and approved this paper.

Funding

Open Access funding enabled and organized by Projekt DEAL.

Competing interests

The authors declare no competing interests.

Additional information

Supplementary information The online version contains supplementary material available at <https://doi.org/10.1038/s43247-023-01158-w>.

Correspondence and requests for materials should be addressed to Simon Thivet.

Peer review information *Communications Earth & Environment* thanks Ilya Vekslar, Alessio Zandona and the other, anonymous, reviewer(s) for their contribution to the peer review of this work. Primary handling editors: Lucia Pappalardo, Joe Aslin, Heike Langenberg. A peer review file is available.

Reprints and permission information is available at <http://www.nature.com/reprints>

Publisher's note Springer Nature remains neutral with regard to jurisdictional claims in published maps and institutional affiliations.



Open Access This article is licensed under a Creative Commons Attribution 4.0 International License, which permits use, sharing, adaptation, distribution and reproduction in any medium or format, as long as you give appropriate credit to the original author(s) and the source, provide a link to the Creative Commons license, and indicate if changes were made. The images or other third party material in this article are included in the article's Creative Commons license, unless indicated otherwise in a credit line to the material. If material is not included in the article's Creative Commons license and your intended use is not permitted by statutory regulation or exceeds the permitted use, you will need to obtain permission directly from the copyright holder. To view a copy of this license, visit <http://creativecommons.org/licenses/by/4.0/>.

© The Author(s) 2023